

Photocatalytic water splitting in (co)doped SrTiO_3 from first principles calculations

Manish Kumar,^{*} Pooja Basera, Shikha Saini, and Saswata Bhattacharya[†]

*Department of Physics, Indian Institute of Technology Delhi,
New Delhi 110016, India*

(Dated: May 9, 2022)

Using the hybrid density functional theory and *ab initio* atomistic thermodynamics, we have investigated the thermodynamic stability of non-metal (N), metal (Mn) related monodoped SrTiO_3 . We find that substitutional defect is the most stable defect over a wide range of environmental conditions relevant to the experimental growth conditions. However, despite substitution of N at O site (N_O) helps in reducing the band gap, it introduces the localized states deep inside the forbidden region that act as recombination centers and degrade the photocatalytic efficiency. On the other hand, in the case of substitution of Mn at Sr site, the band gap (3.25 eV) is not suitable for inducing visible light absorption. However, substitution of Mn at Ti site helps to reduce the band gap (2.57 eV) to visible light absorption but due to shift of conduction band minima in downward direction, its reduction power to produce of H_2 from water splitting is lowered. Thus, monodoping of N or Mn can induce visible light absorption, but none of them are suitable to ameliorate the photocatalytic activity. Therefore, in order to achieve enhanced photocatalytic activity of SrTiO_3 , we have employed codoped Mn and N simultaneously in SrTiO_3 to modulate its electronic properties effectively. In the codoped SrTiO_3 the recombination of photogenerated charge carriers is suppressed, and the diffusion and mobility are increased owing to the passivation of discrete localized states. Our results reveal that $\text{Mn}_{\text{Sr}}\text{N}_\text{O}$ (codoping of Mn at Sr site and N at O site) is the most promising candidate for enhancing the photocatalytic activity of SrTiO_3 under visible light.

I. INTRODUCTION

Semiconductor-based photocatalysts have attracted considerable interest due to their potential in harnessing solar energy for solving the current energy demand and environmental degradation [1–4]. The criteria satisfied by a photocatalyst involve suitable band-edge positions that straddle the reduction and oxidation potential of a desired chemical compound, high separation rate, slow recombination rate, high mobility of photoexcited charge carriers, and longer lifetime. Among various perovskite photocatalysts, SrTiO_3 has emerged as one of the promising material for photocatalytic water splitting and pollutant degradation in the past few decades because of its exceptional electronic structure, optical properties, photochemical stability, and low cost [5–9]. However, one of the major concerns is its large band gap (3.25 eV) due to which it only responds to ultraviolet (UV) irradiation, which consists of only 4% of the solar spectrum [10]. Therefore, it delimits the application of SrTiO_3 on a commercial level. Thus, several works have been endeavored to reduce the band gap of SrTiO_3 in order to induce visible light absorption via doping with metals [11, 12], nonmetals [13, 14] or combination of several elements [15–19].

Earlier, different metal cations, particularly transition metal (TM) dopants, are used to expand the spectral response [11, 20–23]. However, merely the band gap reduction cannot ensure the enhancement in photocatalytic

efficiency. For metal-cation doped SrTiO_3 , TM d-states hybridize with those states of the SrTiO_3 that contribute to conduction band, and thus the reduction in band gap occurs by shifting of conduction band minimum (CBM) in downward direction. However, due to this shift in conduction band edge, the reducing power is deteriorated. Also, deep level traps arise frequently in the forbidden region, which act as recombination centers causing difficulty in separation and migration of photogenerated charge carriers [12, 24]. Therefore, transition metal alone is not suitable for improvement in photocatalytic activity. As a result of the shortcomings from metal dopants, non-metal doping approach is also employed [25–27]. Among the nonmetals doping, N-doped SrTiO_3 is found to narrow the band gap by elevating the valence band maximum (VBM). This is due to the fact that the N (2p) states are higher in energy than the O (2p) states and thus, yields visible light response [26]. However, localized states are appeared deep inside the forbidden region, which can trap the photoexcited charge carriers and accelerate the electron-hole recombination and hence, degrade the photocatalytic efficiency. The codoping with a metal is one of the pre-eminent solutions to passivate the discrete states of non-metal dopants in the forbidden region, and form the continuum band [24, 28–30]. Earlier studies have suggested that codoping of metal in N-doped SrTiO_3 stabilizes the system, i.e., the solubility of N gets increased [24, 28]. By means of codoping, band edges can be engineered to comply with the needs, i.e., the spectral response expands to the visible region while retaining the reduction and oxidation power [31]. The photogenerated charge separation is promoted and recombination is suppressed owing to the internal field developed by relatively large distortion occurrence in case of codoping [28]. In

^{*} Manish.Kumar@physics.iitd.ac.in

[†] saswata@physics.iitd.ac.in

essence, this approach of synergistic codoping enhances the photocatalytic efficiency of SrTiO₃.

In this present article, we have studied the role of monodoping of N (nonmetal) and Mn (metal) as well as the codoping of Mn and N in SrTiO₃ for enhancing the photocatalytic efficiency under visible light. Firstly, the stability of N- and Mn-doped SrTiO₃ has been evaluated using hybrid density functional study and *ab initio* atomistic thermodynamics at realistic conditions (temperature (T) and partial pressure of oxygen (p_{O_2})) [32]. On doping SrTiO₃ with N, the possible defects that could occur are: N_O (N substituted at O position), N_i (N as an interstitial making bond with O), and (N₂)_O split-interstitial (one N is at interstitial position and another one is substituted the nearby O, making bond with each other) [26, 33, 34]. In the case of Mn doping, Mn could be substituted either at Ti (Mn_{Ti}) or Sr (Mn_{Sr}) site, or it could also be present as an interstitial (Mn_i) in SrTiO₃ [35, 36]. These defects are not stable in neutral form because of the charge uncompensation. Therefore, we have calculated the stability of charged defects in addition to neutral defects with charge states q ($-2, -1, 0, +1, +2$). Note that, in order to compensate the charge, one can adapt either of the approaches: (i) explicit presence of oxygen vacancies for the neutral dopants [37, 38] or (ii) addition of external charge to the dopant [32, 39, 40]. Both the approaches yield the same conclusion as they are doing effectively the same charge compensation at the defect site. Further, the formation energy plots tell us that which would be the most prominent charge defect at different environmental conditions, that remove the ambiguity of the preferred defect site in doped SrTiO₃. For the codoping of Mn and N in bulk SrTiO₃, any experimental or theoretical reports are hitherto unknown. Therefore, we present here an indepth theoretical studies on Mn-N codoped SrTiO₃ at a realistic environmental condition (i.e. temperature (T), and pressure (p_{O_2})). To understand the Mn-N codoped case, first we have addressed the respective monodoped cases and its thermodynamic stability at a finite T, p_{O_2} . To get the insights on synergistic effect of codoping, electronic density of states for pristine, monodoped and codoped SrTiO₃ have been compared. In addition to this, the optical response of pristine, N-, Mn-doped and Mn-N codoped SrTiO₃ is also analyzed. Finally, from the perspective of its usage in photocatalytic water splitting, we have examined the band edges alignment of undoped and doped SrTiO₃ w.r.t. water redox potential levels.

II. METHODOLOGY

We have carried out the density functional theory (DFT) [41, 42] calculations using the Vienna *ab initio* simulation package (VASP) [43–46]. The projector-augmented wave (PAW) potentials [47] are used to describe the ion-electron interactions in all the elemental constituents, viz. Sr, Ti, Mn, O, and N, which contains ten, four, seven, six, and five valence electrons, respec-

tively. The total energy calculations are performed using hybrid exchange–correlation (xc) functional HSE06 [48] (for validation of xc functionals, see Sec. I in Supplemental Material (SM)). The screening parameter of 0.2 Å⁻¹ and 28% Hartree-Fock mixing parameter yield the bandgap of 3.28 eV (see Fig. S1(c) in SM), which is in good agreement with the experimental value of 3.25 eV [49]. To introduce defects in SrTiO₃, we have used a 40-atom supercell, which is constructed by a $2 \times 2 \times 2$ repetition of cubic SrTiO₃ unit cell (5 atoms). To ensure the convergence of supercell size, test calculations have been performed with 90-atom supercell ($3 \times 3 \times 2$ repetition of unit cell of SrTiO₃) for the case of N_O in order to ensure that the defect is fully localized. The results obtained from 40- and 90-atom supercells are consistent with each other. Therefore, the results are impervious to the supercell size [50]. A k-point mesh of $4 \times 4 \times 4$ is used, which is generated using Monkhorst-Pack [51] scheme. The self consistency loop is converged with a threshold of 0.01 meV energy. The cutoff energy of 600 eV is used for the plane wave basis set. Note that, we have performed the spin-polarized calculations because the doped systems contain unpaired electrons. The quasiparticle energy calculations have been carried out using single-shot G₀W₀ approximation [52, 53] starting from the orbitals obtained using HSE06 xc functional. The polarizability calculations are performed on a grid of 50 frequency points. To make computation feasible, the number of bands is set to 384, which is typically four times the number of occupied orbitals.

III. RESULTS

A. Stability of defects in SrTiO₃: *ab initio* atomistic thermodynamics

To analyze the thermodynamic stability of defected supercell w.r.t. pristine supercell of SrTiO₃, we have calculated the formation energy by means of *ab initio* atomistic thermodynamics [32, 39, 54, 55]. The defect state that has the lowest formation energy is the most stable defect configuration at a given environmental condition. For N substituted at O in pristine supercell of SrTiO₃ with charge state q , formation energy is calculated as follow [32, 56]:

$$E_f(N_O)^q = E_{\text{tot}}(N_O)^q - E_{\text{tot}}(\text{SrTiO}_3) + \mu_O - \mu_N + q(\mu_e + \text{VBM} + \Delta V), \quad (1)$$

where $E_f(N_O)^q$ is the formation energy for substitution of N at O in pristine supercell. $E_{\text{tot}}(N_O)^q$ and $E_{\text{tot}}(\text{SrTiO}_3)$ are the total energies obtained from DFT with and without defect. μ_O is the chemical potential for oxygen atom, referenced from the total free energy of O₂ molecule at absolute zero, which is obtained from DFT total energy with addition of zero point energy of O₂ molecule, i.e., $\mu_O = \Delta\mu_O + \frac{1}{2}(E_{\text{tot}}(\text{O}_2) + \frac{\hbar\nu_{\text{O}_2}}{2})$. In the latter term,

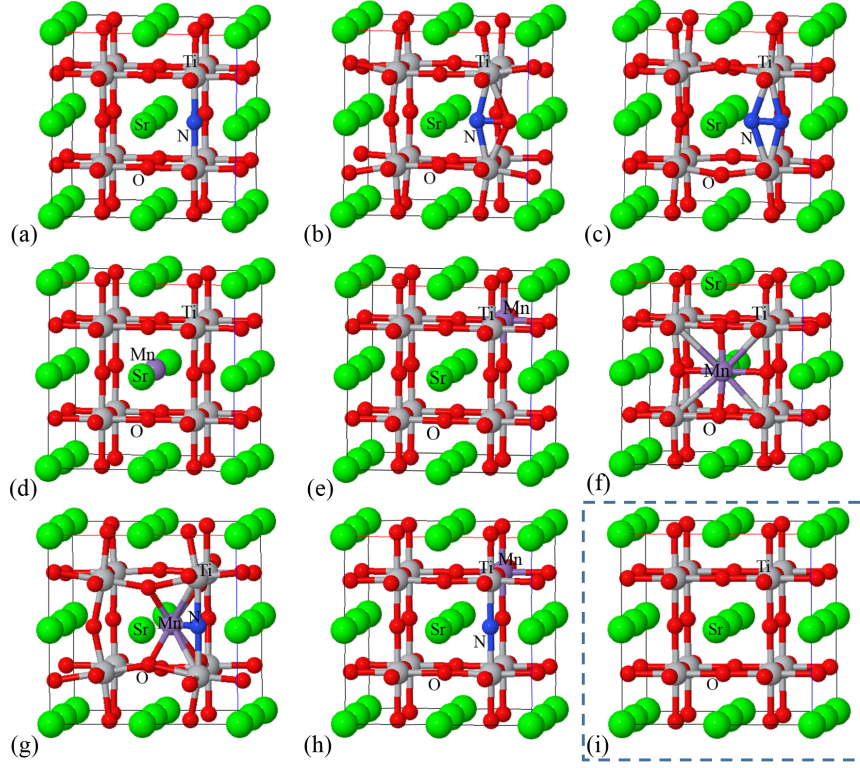


FIG. 1. Ball and stick model of optimized structures of (a) NO, (b) Ni, (c) (N₂)O, (d) MnSr, (e) MnTi, (f) Mn, (g) MnSrNO, (h) MnTiNO, and (i) pristine SrTiO₃.

ν_{OO} is the O-O stretching frequency. Similarly, the chemical potential for Nitrogen atom is calculated by taking the total free energy of N₂ molecule as reference (at absolute zero), i.e., $\mu_{\text{N}} = \Delta\mu_{\text{N}} + \frac{1}{2} (E_{\text{tot}}(\text{N}_2) + \frac{h\nu_{\text{NN}}}{2})$, where ν_{NN} is the N-N stretching frequency. The chemical potentials, $\Delta\mu_{\text{X}}$ (X = O, N, Mn, Sr, and Ti) have been chosen carefully to reflect the appropriate environmental growth conditions. μ_{e} is the chemical potential of electron, which is varied from VBM to CBM of pristine supercell of SrTiO₃ and ΔV accounts for the core level alignment of the defected system w.r.t. pristine neutral. The effect of temperature and pressure is explicitly taken into chemical potential term. The chemical potential $\Delta\mu_{\text{O}}$ as a function of temperature (T) and the partial pressure of oxygen (p_{O_2}) is calculated using the relation [54]:

$$\begin{aligned} \Delta\mu_{\text{O}}(T, p_{\text{O}_2}) = & \frac{1}{2} \left[-k_{\text{B}}T \ln \left[\left(\frac{2\pi m}{h^2} \right)^{\frac{3}{2}} (k_{\text{B}}T)^{\frac{5}{2}} \right] \right. \\ & + k_{\text{B}}T \ln p_{\text{O}_2} - k_{\text{B}}T \ln \left(\frac{8\pi^2 I_A k_{\text{B}}T}{h^2} \right) \\ & + k_{\text{B}}T \ln \left[1 - \exp \left(\frac{-h\nu_{\text{OO}}}{k_{\text{B}}T} \right) \right] \\ & \left. - k_{\text{B}}T \ln \mathcal{M} + k_{\text{B}}T \ln \sigma \right], \end{aligned} \quad (2)$$

where m is the mass, I_A is the moment of inertia of O₂ molecule, \mathcal{M} is the spin multiplicity and σ is the symmetry number.

Under equilibrium growth conditions, the chemical potentials are related to enthalpy of formation of SrTiO₃ ($\Delta H_{\text{f}}(\text{SrTiO}_3)$) by:

$$\Delta\mu_{\text{Sr}} + \Delta\mu_{\text{Ti}} + 3\Delta\mu_{\text{O}} = \Delta H_{\text{f}}(\text{SrTiO}_3). \quad (3)$$

To ensure the suppression of secondary phases, constraints are imposed on the different chemical potentials as given below:

$$\begin{aligned} \Delta\mu_{\text{Ti}} + 2\Delta\mu_{\text{O}} &\leq \Delta H_{\text{f}}(\text{TiO}_2) \\ \Delta\mu_{\text{Sr}} + \Delta\mu_{\text{O}} &\leq \Delta H_{\text{f}}(\text{SrO}) \\ \Delta\mu_{\text{X}} &\leq 0. \end{aligned} \quad (4)$$

We have calculated the formation energy in three regimes, viz. O-rich, O-intermediate and O-poor conditions. Under O-rich condition, $\Delta\mu_{\text{O}} = 0$ eV, $\Delta\mu_{\text{Ti}} = -9.11$ eV, $\Delta\mu_{\text{Sr}} = -8.54$ eV, and $\Delta\mu_{\text{Mn}} = -5.61$ eV. Under O-rich and O-intermediate conditions, $\Delta\mu_{\text{Ti}}$ and $\Delta\mu_{\text{Mn}}$ are limited by the formation of TiO₂ and MnO₂, respectively. In O-intermediate condition, $\Delta\mu_{\text{O}}$ takes the value to reflect the experimental growth condition ($T = 1100$ °C, $p_{\text{O}_2} = 1$ atm [25]). Therefore, in O-intermediate growth condition, $\Delta\mu_{\text{O}} = -1.58$ eV, $\Delta\mu_{\text{Ti}} = -5.95$ eV, $\Delta\mu_{\text{Sr}} = -6.96$ eV, and $\Delta\mu_{\text{Mn}} = -2.44$ eV. Under O-poor

(Ti-rich) condition, $\Delta\mu_{\text{Ti}}$ and $\Delta\mu_{\text{Mn}}$ are limited by the formation of metallic phase of Ti and Mn, respectively. Hence, in O-poor condition, $\Delta\mu_{\text{O}} = -4.55$ eV, $\Delta\mu_{\text{Ti}} = 0$ eV, $\Delta\mu_{\text{Sr}} = -3.98$ eV, and $\Delta\mu_{\text{Mn}} = 0$ eV. We have fixed the $\Delta\mu_{\text{N}} = -1.48$ eV, which is obtained at experimental growth condition. By knowing the stability of different dopants under certain conditions, one could deliberately dope the SrTiO₃ in accordance with the need.

1. N-related Defects

The optimized structures of all the doped and pristine SrTiO₃ supercell are shown in Fig. 1. SrTiO₃ has a cubic structure space group $Pm\bar{3}m$ at room temperature. On doping N in pristine supercell, N-related defects, viz. N_O, N_i, and (N₂)_O could form as shown in Fig. 1(a), 1(b) and 1(c), respectively. N_O shows negligible distortion, whereas N_i and (N₂)_O show more distortion in the lattice. The formation energies of N-related

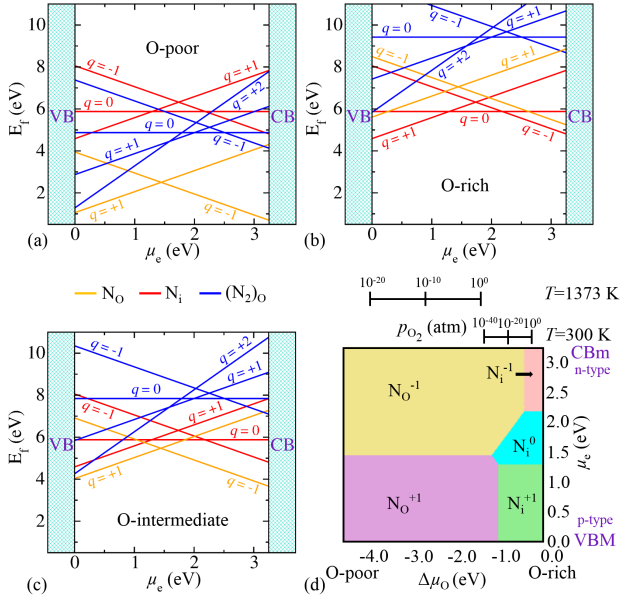


FIG. 2. Formation energy of N-related defects as a function of chemical potential of electron under (a) O-poor, (b) O-rich and (c) O-intermediate condition. (d) 2D projection of the 3D phase diagram that manifests the stable phases of N-related charged defects having minimum formation energy as a function of μ_e and $\Delta\mu_{\text{O}}$. Here, on x-axis, $\Delta\mu_{\text{O}}$ is varied according to T and p_{O_2} , and on y-axis, μ_e is varied from VBM to CBm of pristine SrTiO₃. Colored regions show the most stable phases having minimum formation energy at a given environmental condition. Top axes are showing the pressure (p_{O_2}) range at two temperatures: $T=300$ K and 1373 K.

defects as a function of chemical potential of electron μ_e with different charge states, under different environmental conditions are shown in Fig. 2. Only those charge states of a particular defect are considered that have low formation energy. The charge states $+1$ and -1 are en-

ergetically stable in case of N_O near VBM and CBm, respectively. The interstitial N (N_i) can form bond with O by sharing its lattice site making split-interstitial. N_i is energetically stable in charge states $+1$, 0 , and -1 . We also have found that N_O can make bond with interstitial N forming (N₂)_O split-interstitial. It can be stable in charge states $+2$, $+1$, 0 , and -1 . The positive charge states are more favorable for smaller value of μ_e , i.e., near VBM and negative charge states are stable for larger value of μ_e (near CBm). N_O is the predominant defect in case of O-poor and O-intermediate conditions (Fig. 2(a) and 2(c)), whereas N_i is the stable defect in O-rich condition (Fig. 2(b)). This is attributed by the fact that in O-rich condition, substitution of N at O is difficult because vacancy of O will not be favorable. Also, we have noticed that it is easier to substitute N at O in O-poor condition since it favors the O vacancy. N_O is stable with charge state -1 near CBm as it has one electron less than the O atom. The thermodynamic transition level ($+/-$) lies in between the VBM and CBm indicating that N_O acts both as a deep donor/acceptor depending on the nature of doping (i.e. p-type or n-type). The formation energy of all the N-related defect configurations is large in O-rich and O-intermediate conditions, which implies that N is less soluble in SrTiO₃.

We can sum up about the stability of all the three configurations of N-related defects at different environmental conditions by observing the 3D phase diagram as shown in Fig. 2(d). Here, on x-axis, $\Delta\mu_{\text{O}}$ is varied from O-poor to O-rich condition in accordance with T and p_{O_2} . On y-axis, we have scanned the entire forbidden region by means of μ_e , which is referenced from VBM of pristine SrTiO₃. The smaller (near VBM) and larger (near CBm) values of μ_e correspond to p-type and n-type SrTiO₃, respectively. On z-axis, we have shown the most stable phases having minimum formation energy at a given environmental condition using the colored surfaces. From Fig. 2(d), we can easily see that N_O is the predominant defect in N doped SrTiO₃ for a wide range of environmental conditions including the experimental growth condition ($T = 1373$ K, $p_{\text{O}_2} = 1$ atm), which is in accordance with Fig. 2(a) and 2(c), whereas N_i is only favorable in O-rich condition (also indicated from Fig. 2(b)).

2. Mn-related Defects

On doping Mn in SrTiO₃, the structures that could form are Mn_{Sr}, Mn_{Ti}, and Mn_i as shown in Fig. 1(d), 1(e) and 1(f), respectively. In Fig. 3, the formation energies of Mn-related defects are plotted as a function of chemical potential of electron under the aforementioned environmental conditions. In case of Mn_{Sr}, only neutral defect is stable, which signifies that Mn exists in Mn²⁺ oxidation state when substituted at Sr (Sr²⁺ oxidation state) site in SrTiO₃. Mn_{Ti} is stable with 0 and -1 charge states indicating that in addition to Mn⁴⁺ oxidation state, Mn³⁺ oxidation state could also exist, though

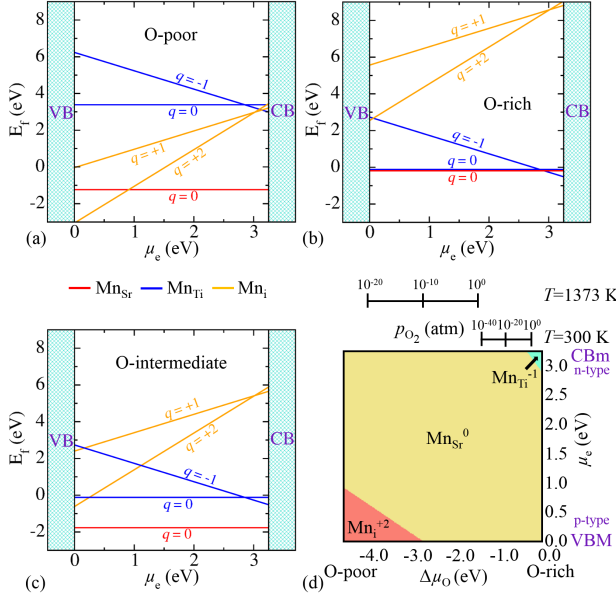


FIG. 3. Formation energy of Mn-related defects as a function of chemical potential of electron under (a) O-poor, (b) O-rich and (c) O-intermediate condition. (d) 2D projection of the 3D phase diagram that manifests the stable phases of Mn-related charged defects having minimum formation energy as a function of μ_e and $\Delta\mu_O$. Here, on x-axis, $\Delta\mu_O$ is varied according to T and p_{O_2} , and on y-axis, μ_e is varied from VBM to CBm of pristine SrTiO_3 . Colored regions show the most stable phases having minimum formation energy at a given environmental condition. Top axes are showing the pressure (p_{O_2}) range at two temperatures: $T=300$ K and 1373 K.

unlikely, when Mn is substituted at Ti (Ti^{4+} oxidation state) site. Mn could also exist as an interstitial (Mn_i) in between the two Sr atoms as shown in Fig. 1(f). Mn_i acts as a donor and is stable in +2 and +1 charge states under O-poor condition. Due to the possibility of Ti vacancy, Mn_{Ti} could be formed under O-rich (Ti-poor) condition, as it is competing with Mn_{Sr} defect in this condition (see Fig. 3(b)). Mn_i with +2 charge state is stable in p-type SrTiO_3 under O-poor condition, while Mn_{Ti} with -1 charge state is stable in n-type SrTiO_3 under O-rich condition as shown in the 3D phase diagram (Fig. 3(d)). Mn_{Sr} in charge state 0 (neutral) is the prominent defect under all the three environmental conditions as shown in Fig. 3(d). The formation energy for Mn doped SrTiO_3 in all oxygen environmental conditions is small, particularly in O-intermediate condition (Fig. 3(c)), which implies that it is easier to dope Mn in SrTiO_3 .

From the above analysis, we conclude that in the case of monodoped SrTiO_3 , substitutional doping is the most stable for a wider region of the environmental conditions including the experimental growth conditions. Therefore, in the following section we have considered only the substitutional position for codoping of Mn and N in SrTiO_3 to understand its efficiency as a potential photocatalyst

for water splitting.

3. Defect pair binding energy

Fig. 1(g) and 1(h) show the optimized structures of Mn-N codoped SrTiO_3 , which are $\text{Mn}_{\text{Sr}}\text{N}_\text{O}$ and $\text{Mn}_{\text{Ti}}\text{N}_\text{O}$, respectively. The binding energy of the defect pairs (Mn + N) in SrTiO_3 has been calculated to see if their formation is stable or not, as follow [29]:

$$E_b = E(\text{Mn}_{\text{Sr}}\text{N}_\text{O}) + E(\text{SrTiO}_3) - E(\text{Mn}_{\text{Sr}}) - E(\text{N}_\text{O}), \quad (5)$$

where E_b is the defect pair binding energy, $E(\text{Mn}_{\text{Sr}})$ is the total energy of SrTiO_3 supercell with Mn substitution at Sr site, $E(\text{N}_\text{O})$ is the total energy of N substituted O in SrTiO_3 supercell, $E(\text{Mn}_{\text{Sr}}\text{N}_\text{O})$ is the total energy of Mn and N codoped (Mn at Sr site and N at O site) SrTiO_3 supercell and $E(\text{SrTiO}_3)$ is the total energy of pristine supercell. A more negative value of E_b indicates more to be the possibility to form defect pair when both the dopants are present in the sample. For $\text{Mn}_{\text{Sr}}\text{N}_\text{O}$ and $\text{Mn}_{\text{Ti}}\text{N}_\text{O}$ pairs, the calculated binding energies E_b are -1.46 and -0.33 eV, respectively. These values indicate that defect pairs are more stable than the isolated impurities in SrTiO_3 supercell. Also, $\text{Mn}_{\text{Sr}}\text{N}_\text{O}$ is more stable configuration than $\text{Mn}_{\text{Ti}}\text{N}_\text{O}$ since $\text{Mn}_{\text{Sr}}\text{N}_\text{O}$ has higher (more negative) binding energy E_b than $\text{Mn}_{\text{Ti}}\text{N}_\text{O}$. In the codoped system, Mn acts as a donor, whereas N acts as an acceptor. The charge transfer takes place from donor to acceptor and strong Coulomb interaction arises between positively charged donor and negatively charged acceptor. Hence, the defect pair is stable. The extra stability in $\text{Mn}_{\text{Sr}}\text{N}_\text{O}$ is due to the shift of Mn away from the Sr centre towards N as shown in Fig. 1(g) and making strong bonds with its neighbor atoms.

B. Electronic density of states (DOS)

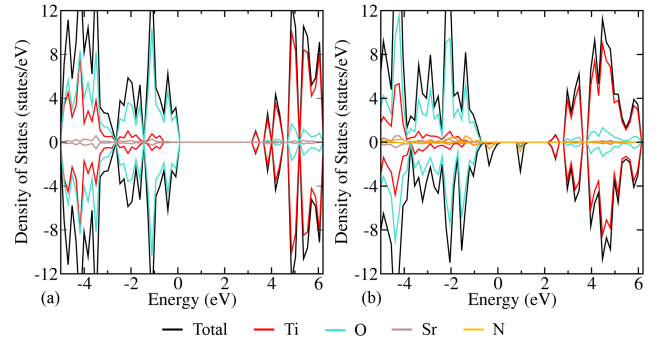


FIG. 4. Electronic density of states for the supercell of (a) pristine SrTiO_3 and (b) N_O type defect.

To get more insights about the effect of dopants in SrTiO_3 , we have calculated atom projected density of

states (pDOS). In Fig. 4(a), we show the density of states for pristine SrTiO_3 . In pristine case, the O 2p orbitals contribute to VBM, and Ti 3d orbitals contribute to CBM with a wide band gap of 3.28 eV. The density of states are symmetric w.r.t. spin alignments (i.e. spin up or down). This confirms that the pristine SrTiO_3 is non-magnetic. We have computed then the DOS for N_O defect in SrTiO_3 , which is shown in Fig. 4(b). On substituting N at O site, some occupied states are appeared above pristine-VBM and some unoccupied discrete states can also be seen deep inside the forbidden region (since the N 2p orbitals have higher energy than the O 2p orbitals). This results in reduction of band gap. The DOS is asymmetrical w.r.t. spin up and spin down contribution due to devoid of an electron in comparison to pristine SrTiO_3 . The midgap states increase the recombination rate and decrease the charge mobility that leads to degradation of photocatalytic activity. Hence, we have used Mn simultaneously as a codopant to passivate the aforementioned discrete midgap states.

We have considered two sites for the substitution of Mn,

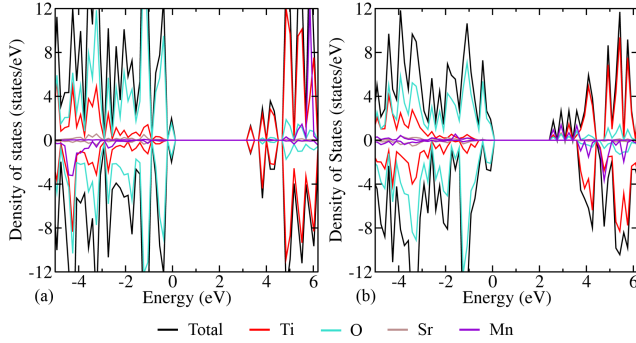


FIG. 5. Electronic density of states for (a) Mn_{Sr} and (b) Mn_{Ti} in the supercell of SrTiO_3 .

viz. Sr and Ti sites as shown in Fig. 1(d) and 1(e), respectively. In case of monodoping of Mn at Sr site, the band gap (3.25 eV) is not getting reduced as shown in Fig. 5(a) and thus, cannot induce visible light absorption. The occupied and unoccupied states of Mn orbital are appeared deep inside the valence and conduction band respectively, indicating that Mn_{Sr} is very stable. Thus, in this case, Mn makes strong bonds with its neighbor atoms. However, in case of Ti site substitution, we get interesting feature in the DOS. The localized states brings down the CBM as shown in Fig. 5(b). Hence, the band gap is reduced to 2.57 eV, resulting in the visible light absorption. However, due to shift of CBM in downward direction, its reduction power is lowered. Therefore, it can not be a potential candidate for H_2 production from water splitting.

In case of codoping, the substitution of Mn at both sites, Sr and Ti in addition to N_O , helps in passivating the localized mid gap states, which are introduced by N substitution, and form continuum states as shown in Fig. 6. The passivation of states is concomitant with the hy-

bridization of O and N orbitals, and Mn and O orbitals in $\text{Mn}_{\text{Sr}}\text{N}_\text{O}$ defect configuration as shown in Fig. 6(a') (near VBM). However, in the case of $\text{Mn}_{\text{Ti}}\text{N}_\text{O}$, Mn states arise only near CBM as shown in Fig. 6(b'). The recombination of photogenerated charge carriers is suppressed, and the diffusion and mobility are increased owing to the passivation of discrete localized states. The band gaps of $\text{Mn}_{\text{Sr}}\text{N}_\text{O}$ and $\text{Mn}_{\text{Ti}}\text{N}_\text{O}$ are 2.17 and 1.94 eV, respectively, which are the desirable one for visible light absorption. In case of $\text{Mn}_{\text{Ti}}\text{N}_\text{O}$, CBM is shifted downward by a large amount and hence, adversely affect the reduction power for hydrogen generation, whereas in case of $\text{Mn}_{\text{Sr}}\text{N}_\text{O}$, this downward shift is very small. Consequently, the codoping of Mn at Sr site and N at O site is favorable for H_2 generation from photocatalytic water splitting. Also, from Fig. 1(g), we can see a relatively large distortion in case of $\text{Mn}_{\text{Sr}}\text{N}_\text{O}$ codoping, which builds up the internal field, that is helpful for photogenerated charge carriers separation and thus, enhances the photocatalytic efficiency. Therefore, $\text{Mn}_{\text{Sr}}\text{N}_\text{O}$ codoping in SrTiO_3 is the promising candidate to enhance the photocatalytic efficiency and generate hydrogen from water splitting.

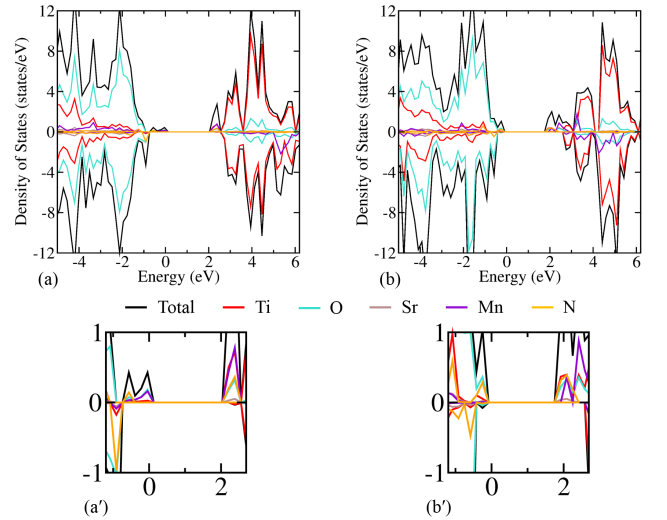


FIG. 6. Electronic density of states for (a) $\text{Mn}_{\text{Sr}}\text{N}_\text{O}$ and (b) $\text{Mn}_{\text{Ti}}\text{N}_\text{O}$ in the supercell of SrTiO_3 . (a') and (b') are the magnified images of (a) and (b), respectively.

C. Optical properties

To determine the optical spectra, we have computed the frequency dependent complex dielectric function that can be written as $\epsilon(\omega) = \epsilon_1(\omega) + i\epsilon_2(\omega)$ using the GW approach. The real (ϵ_1) and imaginary (ϵ_2) part of dielectric function have shown in Fig. 7(a) and 7(b), respectively. The static ($\omega = 0$) real part of $\epsilon(\omega)$ for pristine SrTiO_3 is found to be 3.46 which is well in agreement with previous findings [57] of Ergönenc *et al.* On doping, its value is increased. At $\omega = 0$, $\epsilon_1(\omega)$ has the value of

3.61, 3.66, 3.72, 3.48 and 3.54 for N_O , Mn_Ti , $\text{Mn}_\text{Ti}\text{N}_\text{O}$, Mn_Sr and $\text{Mn}_\text{Sr}\text{N}_\text{O}$, respectively (Fig. 7(a)). The imaginary part of dielectric function represents the optical absorption (Fig. 7(b)). We have found the first peak at 4.20 eV for pristine SrTiO_3 , while experimentally, it is at 4.7 eV [58]. This discrepancy between theoretical and experimental value may be arises due to electron-phonon coupling and/or choice of pseudopotentials. For doped SrTiO_3 , the first peaks are at 4.11 eV, 4.13 eV, 4.02 eV, 4.22 eV and 4.18 eV for N_O , Mn_Ti , $\text{Mn}_\text{Ti}\text{N}_\text{O}$, Mn_Sr and $\text{Mn}_\text{Sr}\text{N}_\text{O}$, respectively. Note that the peaks are shifted towards lower energy region. Even if the exact numbers may vary w.r.t. experiments, atleast from the trends it's clear that the band gap is getting reduced on doping in SrTiO_3 . Also, we could note that the onset of the absorption edge is shifting towards the lower region. Hence, the optical response is shifted towards the visible region. The dielectric function obtained using HSE06 have been provided in SM (see Fig. S3 in SM). The peak positions are at almost same energy values with higher intensity in comparison to the values obtained from GW. We have found that except Mn_Sr , all dopants induce visible light response (see Fig. S2 in SM). The spectra of Mn_Sr coincides with the pristine supercell of SrTiO_3 because there is no reduction in band gap on substituting Mn at Sr site, while in rest of the cases, band gap is reduced (see Fig. 7(b)).

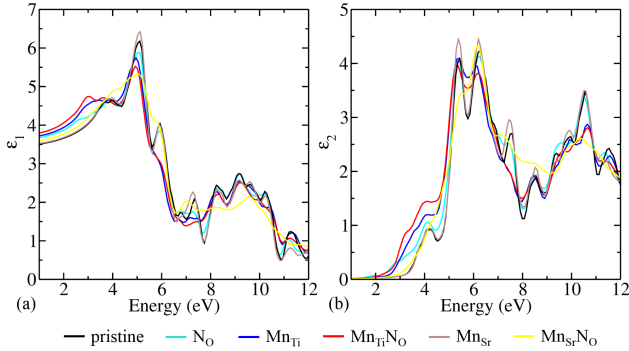


FIG. 7. Spatially average (a) real (ϵ_1) and (b) imaginary (ϵ_2) part of the dielectric function obtained by G_0W_0 @HSE06 for the pristine, monodoped and codoped SrTiO_3 .

D. Band edge alignment

We have seen that the doping helps in reducing the band gap and induces visible light response. However, only reduction in band gap can not assure the hydrogen generation via photocatalytic water splitting. The band edges (VBM and CBm) should have appropriate position. For water splitting, the CBm must lie above the water reduction potential level (H^+/H_2) and VBM must be positioned below water oxidation potential level ($\text{O}_2/\text{H}_2\text{O}$). Firstly, we have aligned the band edges of undoped SrTiO_3 w.r.t. water redox potential levels. The

CBm lies 0.8 eV above the water reduction potential (H^+/H_2) and VBM lies 1.25 eV below water oxidation potential [59]. Thereafter, we align the band edges of doped SrTiO_3 by observing the shift in energy of the VBM and CBm w.r.t. undoped SrTiO_3 . From Fig. 8, we have found that in the case of N_O , the VBM is shifted upwards and the CBm is not disturbed. But some localized states are present deep in the forbidden region, which degrades the photocatalytic efficiency. Hence, N_O is not the promising one for water splitting. In case of Mn_Ti and $\text{Mn}_\text{Ti}\text{N}_\text{O}$, the CBm is shifted downward by a large amount and hence, their reduction power is very low and could not be utilized for hydrogen generation from water. On substituting Mn at Sr site, the band gap is not getting reduced and thus, not inducing the visible spectrum response. Therefore, $\text{Mn}_\text{Sr}\text{N}_\text{O}$ system is the most promising one, because in this case, CBm is shifted by small amount and also, it has large defect pair binding energy. It has a desirable band gap of 2.17 eV and also, does not contain any localized midgap states. In view of this, we have seen that all the defect configurations except Mn_Sr induce spectral response in visible region, but from the applicability in photocatalytic water splitting, only $\text{Mn}_\text{Sr}\text{N}_\text{O}$ is the most desirable one. Hence, these theoretical studies help in further future investigation theoretically as well as experimentally to engineer a device that will be environment friendly.

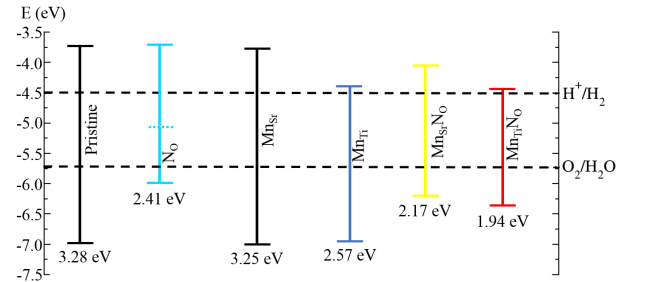


FIG. 8. Band edge alignment of (un)doped SrTiO_3 w.r.t. water redox potential levels (H^+/H_2 , $\text{O}_2/\text{H}_2\text{O}$).

IV. CONCLUSIONS

In summary, we have systematically studied the thermodynamic stability of different types of dopants and codopants in SrTiO_3 using hybrid DFT and *ab initio* thermodynamics. We have found that hybrid functional HSE06 is essential to address the system, where DFT with local/semi-local functionals is totally insufficient even for a qualitative analysis. We have observed that substitutional defects viz. N_O and Mn_Sr are the most stable ones in case of monodoping under equilibrium growth conditions in SrTiO_3 . However, despite substitution of N at O site (N_O) helps in reducing the band gap, it generates localized states deep inside the band gap. These

states act as recombination centers, which in turn reduce the photocatalytic efficiency. On the other hand, for substitution of Mn at Sr site, the band gap (3.25 eV) is too large and it falls outside the scope of visible light absorption. However, substitution of Mn at Ti site helps to reduce the band gap (2.57 eV) to visible light absorption. But in this case, due to shift of conduction band minima in downward direction, its reduction power to produce of H_2 from water splitting is lowered. Thus, monodoping of both N or Mn can induce visible light absorption, but none of them are suitable for photocatalytic activity. The codoping of Mn in N-doped $SrTiO_3$ increases the solubility of N in $SrTiO_3$. Moreover, the codoping reduces the band gap to ideal visible region as well as passivates the localized states to form the continuous band with suitable band edge positions. We find that $Mn_{Sr}N_O$ is more stable defect configuration than $Mn_{Ti}N_O$. Our results indicate

that $Mn_{Sr}N_O$ codoped $SrTiO_3$ could be a potential candidate for producing hydrogen via photocatalytic water splitting.

V. ACKNOWLEDGEMENT

MK acknowledges CSIR, India, for the junior research fellowship [grant no. 09/086(1292)/2017-EMR-I]. PB acknowledges UGC, India, for the senior research fellowship [grant no. 20/12/2015(ii)EUV]. SS acknowledges CSIR, India, for the senior research fellowship [grant no. 09/086(1231)/2015-EMR-I]. SB acknowledges the financial support from YSS-SERB research grant, DST, India (grant no. YSS/2015/001209). We acknowledge the High Performance Computing (HPC) facility at IIT Delhi for computational resources.

-
- [1] X. Chen, S. Shen, L. Guo, and S. S. Mao, *Chemical Reviews* **110**, 6503 (2010).
 - [2] C. Chen, W. Ma, and J. Zhao, *Chem. Soc. Rev.* **39**, 4206 (2010).
 - [3] A. Kudo and Y. Miseki, *Chem. Soc. Rev.* **38**, 253 (2009).
 - [4] A. Kubacka, M. Fernández-García, and G. Colón, *Chemical Reviews* **112**, 1555 (2012).
 - [5] K. Domen, A. Kudo, T. Onishi, N. Kosugi, and H. Kuroda, *The Journal of Physical Chemistry* **90**, 292 (1986).
 - [6] S. Ahuja and T. Kutty, *Journal of Photochemistry and Photobiology A: Chemistry* **97**, 99 (1996).
 - [7] K. Iwashina and A. Kudo, *Journal of the American Chemical Society* **133**, 13272 (2011).
 - [8] Q. Zhang, Y. Huang, L. Xu, J.-j. Cao, W. Ho, and S. C. Lee, *ACS Applied Materials & Interfaces* **8**, 4165 (2016).
 - [9] R. Niishiro, S. Tanaka, and A. Kudo, *Applied Catalysis B: Environmental* **150-151**, 187 (2014).
 - [10] P. Kanhere and Z. Chen, *Molecules* **19**, 19995 (2014).
 - [11] R. Konta, T. Ishii, H. Kato, and A. Kudo, *The Journal of Physical Chemistry B* **108**, 8992 (2004).
 - [12] H.-C. Chen, C.-W. Huang, J. C. S. Wu, and S.-T. Lin, *The Journal of Physical Chemistry C* **116**, 7897 (2012).
 - [13] P. Liu, J. Nisar, B. Pathak, and R. Ahuja, *International Journal of Hydrogen Energy* **37**, 11611 (2012).
 - [14] Y. Guo, X. Qiu, H. Dong, and X. Zhou, *Phys. Chem. Chem. Phys.* **17**, 21611 (2015).
 - [15] P. Reunchan, S. Ouyang, N. Umezawa, H. Xu, Y. Zhang, and J. Ye, *J. Mater. Chem. A* **1**, 4221 (2013).
 - [16] S. Ouyang, H. Tong, N. Umezawa, J. Cao, P. Li, Y. Bi, Y. Zhang, and J. Ye, *Journal of the American Chemical Society* **134**, 1974 (2012).
 - [17] B. Modak and S. K. Ghosh, *Phys. Chem. Chem. Phys.* **20**, 20078 (2018).
 - [18] M. Miyauchi, M. Takashio, and H. Tobimatsu, *Langmuir* **20**, 232 (2004).
 - [19] W. Chen, H. Liu, X. Li, S. Liu, L. Gao, L. Mao, Z. Fan, W. Shangguan, W. Fang, and Y. Liu, *Applied Catalysis B: Environmental* **192**, 145 (2016).
 - [20] R. Niishiro, H. Kato, and A. Kudo, *Phys. Chem. Chem. Phys.* **7**, 2241 (2005).
 - [21] H. Yu, S. Ouyang, S. Yan, Z. Li, T. Yu, and Z. Zou, *J. Mater. Chem.* **21**, 11347 (2011).
 - [22] S. Kawasaki, K. Nakatsuji, J. Yoshinobu, F. Komori, R. Takahashi, M. Lippmaa, K. Mase, and A. Kudo, *Applied Physics Letters* **101**, 033910 (2012).
 - [23] P. Li, C. Liu, G. Wu, Y. Heng, S. Lin, A. Ren, K. Lv, L. Xiao, and W. Shi, *RSC Adv.* **4**, 47615 (2014).
 - [24] W. Wei, Y. Dai, M. Guo, L. Yu, and B. Huang, *The Journal of Physical Chemistry C* **113**, 15046 (2009).
 - [25] J. Wang, S. Yin, M. Komatsu, Q. Zhang, F. Saito, and T. Sato, *Journal of Photochemistry and Photobiology A: Chemistry* **165**, 149 (2004).
 - [26] Y. Y. Mi, S. J. Wang, J. W. Chai, J. S. Pan, C. H. A. Huan, Y. P. Feng, and C. K. Ong, *Applied Physics Letters* **89**, 231922 (2006).
 - [27] C. Zhang, Y. Jia, Y. Jing, Y. Yao, J. Ma, and J. Sun, *Computational Materials Science* **79**, 69 (2013).
 - [28] W. Wei, Y. Dai, M. Guo, L. Yu, H. Jin, S. Han, and B. Huang, *Phys. Chem. Chem. Phys.* **12**, 7612 (2010).
 - [29] Y. Gai, J. Li, S.-S. Li, J.-B. Xia, and S.-H. Wei, *Phys. Rev. Lett.* **102**, 036402 (2009).
 - [30] B. Modak and S. K. Ghosh, *The Journal of Physical Chemistry C* **119**, 7215 (2015).
 - [31] B. Modak and S. K. Ghosh, *The Journal of Physical Chemistry C* **119**, 23503 (2015).
 - [32] S. Bhattacharya, D. Berger, K. Reuter, L. M. Ghiringhelli, and S. V. Levchenko, *Phys. Rev. Materials* **1**, 071601 (2017).
 - [33] T. Sun and M. Lu, *Applied Surface Science* **274**, 176 (2013).
 - [34] C. M. Liu, X. T. Zu, and W. L. Zhou, *Journal of Physics D: Applied Physics* **40**, 7318 (2007).
 - [35] A. Tkach, P. M. Vilarinho, and A. L. Kholkin, *Acta Materialia* **53**, 5061 (2005).
 - [36] H. Yang, P. G. Kotula, Y. Sato, M. Chi, Y. Ikuhara, and N. D. Browning, *Materials Research Letters* **2**, 16 (2014).
 - [37] C. D. Valentin, E. Finazzi, G. Pacchioni, A. Selloni, S. Livraghi, M. C. Paganini, and E. Giamello, *Chemical Physics* **339**, 44 (2007).
 - [38] C. Di Valentin, G. Pacchioni, and A. Selloni, *Chemistry of Materials* **17**, 6656 (2005).

- [39] A. Bhattacharya and S. Bhattacharya, Phys. Rev. B **94**, 094305 (2016).
- [40] P. Basera, S. Saini, E. Arora, A. Singh, M. Kumar, and S. Bhattacharya, Scientific reports **9**, 1 (2019).
- [41] P. Hohenberg and W. Kohn, Phys. Rev. **136**, B864 (1964).
- [42] W. Kohn and L. J. Sham, Phys. Rev. **140**, A1133 (1965).
- [43] G. Kresse and J. Hafner, Phys. Rev. B **47**, 558 (1993).
- [44] G. Kresse and J. Furthmüller, Computational Materials Science **6**, 15 (1996).
- [45] G. Kresse and J. Furthmüller, Phys. Rev. B **54**, 11169 (1996).
- [46] G. Kresse and D. Joubert, Phys. Rev. B **59**, 1758 (1999).
- [47] P. E. Blöchl, Phys. Rev. B **50**, 17953 (1994).
- [48] A. V. Krukau, O. A. Vydrov, A. F. Izmaylov, and G. E. Scuseria, The Journal of Chemical Physics **125**, 224106 (2006).
- [49] K. van Benthem, C. Elsässer, and R. H. French, Journal of Applied Physics **90**, 6156 (2001).
- [50] P. Reunchan, N. Umezawa, S. Ouyang, and J. Ye, Phys. Chem. Chem. Phys. **14**, 1876 (2012).
- [51] H. J. Monkhorst and J. D. Pack, Phys. Rev. B **13**, 5188 (1976).
- [52] L. Hedin, Phys. Rev. **139**, A796 (1965).
- [53] M. S. Hybertsen and S. G. Louie, Phys. Rev. Lett. **55**, 1418 (1985).
- [54] S. Bhattacharya, S. V. Levchenko, L. M. Ghiringhelli, and M. Scheffler, New Journal of Physics **16**, 123016 (2014).
- [55] E. Arora, S. Saini, P. Basera, M. Kumar, A. Singh, and S. Bhattacharya, The Journal of Physical Chemistry C **123**, 62 (2019).
- [56] C. Freysoldt, B. Grabowski, T. Hickel, J. Neugebauer, G. Kresse, A. Janotti, and C. G. Van de Walle, Rev. Mod. Phys. **86**, 253 (2014).
- [57] Z. Ergönenc, B. Kim, P. Liu, G. Kresse, and C. Franchini, Phys. Rev. Materials **2**, 024601 (2018).
- [58] M. Cardona, Phys. Rev. **140**, A651 (1965).
- [59] Y. Xu and M. A. A. Schoonen, American Mineralogist **85**, 543 (2000).

Photocatalytic water splitting in (co)doped SrTiO₃ from first principles calculations

Manish Kumar*, Pooja Basera, Shikha Saini, Saswata Bhattacharya*

Department of Physics, Indian Institute of Technology Delhi, New Delhi 110016 India

*Email: Manish.Kumar@physics.iitd.ac.in [MK], saswata@physics.iitd.ac.in [SB]

Supplemental Material

- I. Effect of functionals on phase diagrams.
- II. Optical Properties using HSE06.

I. EFFECT OF FUNCTIONALS ON PHASE DIAGRAMS

We have benchmarked the exchange-correlation (xc) functionals viz. local-density approximation (LDA [1]), semi-local generalized gradient approximation (PBE [2]) and a more pronounced non-local hybrid functional HSE06 [3] to ensure that our results are not an artifact of chosen treatment for the xc. The LDA and PBE functionals underestimate the band gap, giving a value of 1.74 eV and 1.82 eV respectively. While, the hybrid functional HSE06 reproduce the band gap of 3.28 eV by taking the 28% of Hartree-Fock exact exchange into account, which is in nice match with the experimental value of 3.25 eV [4]. We have also calculated the defect formation energy for single oxygen vacancy $E_f(\square)^q$ in our system with charge $q = 0, +1, +2, -1$, and -2 using LDA, PBE and HSE06 functionals, since we have to find out the stability of defects as well as the other energetics. The $E_f(\square)^q$ has been calculated as follow [5, 6]:

$$E_f(\square)^q = E_{\text{tot}}(\square)^q - E_{\text{tot}}(\text{SrTiO}_3) + \mu_{\text{O}} + q(\mu_e + \text{VBM} + \Delta V), \quad (1)$$

where $E_{\text{tot}}(\square)^q$ is the total energy of supercell containing single oxygen vacancy with charge state q , and $E_{\text{tot}}(\text{SrTiO}_3)$ is the total energy of the same supercell without any defect. μ_{O} is the chemical potential of the oxygen atom, which is equal to the energy required to remove one O atom from the pristine supercell and put it into the O reservoir; $\mu_{\text{O}} = \frac{1}{2}E_{\text{tot}}(\text{O}_2)$, and $E_{\text{tot}}(\text{O}_2)$ is the total energy of isolated O_2 molecule. μ_e is the chemical potential of electron, that is referenced from VBM of the pristine supercell. ΔV is the core level alignment between the supercells with and without defect.

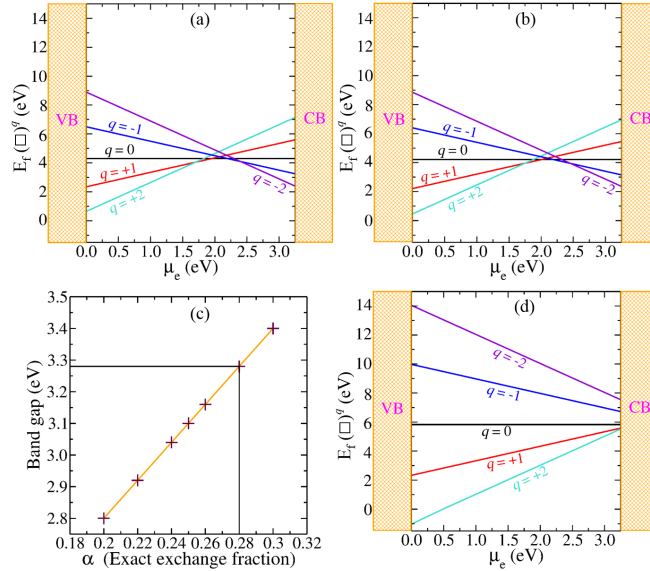


Figure S1: Formation energy of single oxygen vacancy defect as a function of chemical potential of electron under O-rich condition using (a) LDA, (b) PBE, and (d) HSE06 xc functional. (c) represents the variation of bandgap of pristine supercell as a function of exact exchange fraction contained in HSE06 functional.

We have found from figure S1 that $q = +2$ and $q = -2$ are the stable charge states near VBM and CBm respectively using both LDA and PBE functionals. However, this is not the case with hybrid functional HSE06. With HSE06, we have observed that only $q = +2$ charge state is stable throughout the band gap. It implies that, results which are obtained from LDA, PBE xc functionals are different from the HSE06 functional. And as a matter of fact, HSE06 functional is more accurate being non-local and containing a fraction of exact exchange, HSE06 xc functional is more reliable for our system. Therefore, we have done our further calculations with HSE06 functional.

II. OPTICAL PROPERTIES USING HSE06

The real part $\epsilon_1(\omega)$ is calculated using the Kramers-Kronig transformation, and the imaginary part $\epsilon_2(\omega)$ is evaluated by taking summation over large number of empty states as implemented in VASP. The absorption coefficient $\alpha(\omega)$ is

related to real and imaginary part of dielectric function as follow:

$$\alpha(\omega) = \sqrt{2} \omega \left(\sqrt{\epsilon_1(\omega)^2 + \epsilon_2(\omega)^2} - \epsilon_1(\omega) \right)^{\frac{1}{2}}. \quad (2)$$

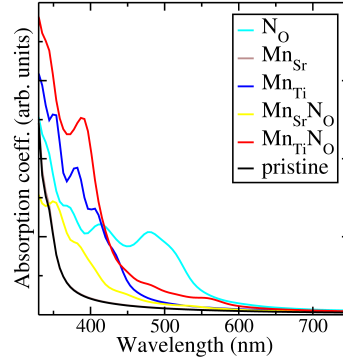


Figure S2: Absorption plot for undoped, monodoped and codoped SrTiO₃ using HSE06 functional.

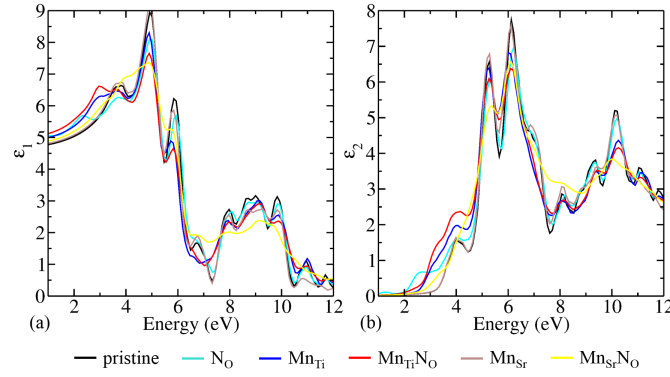


Figure S3: Spatially average (a) real (ϵ_1) and (b) imaginary (ϵ_2) part of the dielectric function obtained by HSE06 for the pristine, monodoped and codoped SrTiO₃.

References

-
- [1] Perdew, J. P. & Wang, Y. Accurate and simple analytic representation of the electron-gas correlation energy. *Phys. Rev. B* **45**, 13244–13249 (1992).
 - [2] Perdew, J. P., Burke, K. & Ernzerhof, M. Generalized gradient approximation made simple. *Phys. Rev. Lett.* **77**, 3865–3868 (1996).
 - [3] Krukau, A. V., Vydrov, O. A. and Izmaylov, A. F. & Scuseria, G. E. Influence of the exchange screening parameter on the performance of screened hybrid functionals. *The J. Chem. Phys.* **125**, 224106 (2006).
 - [4] van Benthem, K., Elsässer, C. & French, R. H. Bulk electronic structure of SrTiO₃: Experiment and theory. *J. Appl. Phys.* **90**, 6156–6164 (2001).
 - [5] Bhattacharya, S., Berger, D., Reuter, K., Ghiringhelli, L. M. & Levchenko, S. V. Theoretical evidence for unexpected O-rich phases at corners of MgO surfaces. *Phys. Rev. Mater.* **1**, 071601 (2017).
 - [6] Freysoldt, C., Grabowski, B., Hickel, T., Neugebauer, J., Kresse, G., Janotti, A. & Van de Walle, C. G. First-principles calculations for point defects in solids. *Rev. Mod. Phys.* **86**, 253 (2014).